Applied Acoustics 245 (2026) 111187

Contents lists available at ScienceDirect

Applied Acoustics

journal homepage: www.elsevier.com/locate/apacoust

Aircraft noise propagation under realistic atmospheric conditions: Comparison of a ray-tracing model with in-situ measurements

Bill Kayser[a,*], Didier Dragna[b]

[a] Cerema, Université Gustave Eiffel, UMRAE, 11 rue Jean Mentelin, 67200, Strasbourg, France
[b] Ecole Centrale de Lyon, CNRS, Université Claude Bernard Lyon 1, INSA Lyon, LMFA, UMR5509, 69130, Ecully, France

HIGHLIGHTS

- Comparison of results from a ray-tracing model and real aircraft noise measurements.
- Inclusion of coherence loss due to atmospheric turbulence scattering in ray-tracing model.
- Accounting for meteorological effects improves agreement with measurements.

ARTICLE INFO

Keywords:
Aircraft noise
Ray tracing
Source in motion
Measurement campaign
Atmospheric turbulence scattering

ABSTRACT

A ray-based numerical model for aircraft noise propagation that accounts for source motion, ground effects, and atmospheric effects as recently proposed (Kayser et al., 2024, Acta Acustica, 8, 62) is evaluated against measurements. Prior to this comparison, an extension of the model is introduced to incorporate coherence loss due to atmospheric turbulence scattering. To capture realistic conditions, noise of aircraft flyovers was recorded on-site, along with aircraft trajectory and meteorological data, including wind and temperature profiles. The spectrograms at 1.2 m above the ground are extrapolated from the measured spectrograms at the ground level using a transfer function computed from both the proposed ray-tracing model and an existing heuristic model from the literature, which neglects refraction. Comparison with the spectrograms measured at 1.2 m shows that both models are capable of reproducing the spectrograms with good accuracy. However, the ray-based model demonstrates greater precision in capturing interference patterns, particularly when the aircraft is not directly overhead relative to the receiver (i.e., for *slant* propagation), where refraction plays a more significant role.

1. Introduction

Aircraft noise prediction requires a precise description of the sound propagation, in addition to source models. Indeed, propagation in the atmosphere is strongly affected by ground reflection, atmospheric stratification, and turbulence-induced scattering. For a moving acoustic source, such as an aircraft, these environmental effects must be considered in addition to Doppler shifts and convective amplification, resulting in complex propagation scenarios. Consequently, significant uncertainties can arise in sound pressure level (SPL) estimations, particularly when using simplified models that neglect certain propagation effects.

While aircraft community noise mostly relies on engineering models, recent studies [1–5] have sought to include meteorological effects using ray-tracing approaches. For aircraft flyover auralization, it is also important to rely on physical models to improve the accuracy of the generated signals. Thus, ray-tracing techniques have also been proposed to simulate the perceptual rendering of aircraft flyovers in realistic environments [6–8]. In addition, the impact of atmospheric turbulence has been addressed in terms of coherence loss between the direct and reflected waves [9,10]. More recently, acoustic scintillation, which induces random fluctuations in the sound pressure amplitude, has also been accounted for via semi-empirical modeling [11].

Another application in which an accurate prediction of sound propagation is critical is aircraft noise certification, where regulatory thresholds impose a decibel-level precision [12]. In this framework, improved modeling tools can support the design of more robust measurement procedures, for instance enabling noise measurements directly at ground level [13–16], and numerically extrapolating the SPL at the standard height of 1.2 m, using a computed transfer function. This approach

---

[*] Corresponding author.
Email address: bill.kayser@cerema.fr (B. Kayser).

https://doi.org/10.1016/j.apacoust.2025.111187
Received 30 June 2025; Received in revised form 25 November 2025; Accepted 27 November 2025

allows bypassing the ground effect contributions in measurements, making it possible to compute them a posteriori through numerical models. As a result, the influence of ground properties can be better controlled and standardized across measurements, ultimately reducing uncertainty and improving the repeatability of acoustic assessment protocols. In order to overcome current model limitations, there is a growing interest in developing more realistic numerical methods, while maintaining low calculation costs, capable of accounting for the combined influence of source motion and atmospheric conditions.

Early studies focused on the development of analytical formulations for a point source moving rectilinearly above a ground surface in a homogeneous and quiescent atmosphere [17–20]. One notable approach is the so-called Dopplerized Weyl–Van der Pol formulation, which allows for a closed-form solution. In the general case of arbitrary motion above a ground surface, no exact analytical solution is available in the literature. However, a heuristic formulation has been introduced in Ref. [21], still for a homogeneous and quiescent atmosphere. To account for meteorological effects on sound propagation, numerical methods are required. While wave-based approaches can be used [22,23], they remain computationally expensive when dealing with moving sources in complex environments.

Recently, we have proposed a coupled formulation combining the heuristic formulation of Ref. [21], which incorporates ground effects at Doppler-shifted frequencies and convective amplification due to source motion, with a ray-tracing (RT) model that determines sound paths in the presence of atmospheric refraction [24]. The developed model thus accounts for the main physical phenomena influencing sound propagation, including source motion (Doppler shift and convective amplification), ground reflection with admittance evaluated at Doppler-shifted frequencies [25], and atmospheric refraction through ray-path curvature and travel-time effects. As a ray-based method, the model offers reasonable computational cost and simpler implementation compared to full wave-based solvers, making it well suited for practical applications. Furthermore, it provides a more physically consistent description of the sound field than quasi-static source models typically used in industrial practice. While the model has shown good agreement with numerical benchmarks in idealized configurations, its application to realistic aircraft scenarios requires an assessment against experimental data which is the purpose of this work.

In this study, we present an in situ validation of the RT-based model using a dedicated measurement campaign. Aircraft performed repeated flyovers along a controlled trajectory, during which acoustic signals were recorded simultaneously at two microphone heights ($z = 0$ m and $z = 1.2$ m) and complemented by meteorological data (wind and temperature profiles) acquired via lidar and radiosonde-equipped drone flights. We also integrate into the RT model coherence loss due to atmospheric turbulence scattering, following a formulation recently proposed for slant propagation [26]. The results of the ray-based simulations are compared to the experimental data and also to predictions from the heuristic formulation in Ref. [21] that neglects atmospheric refraction. The comparison focuses both on the spectrograms recorded at the two microphone heights and on the transfer functions between the microphones. Three test cases under varying atmospheric conditions were selected for detailed comparison.

The paper is organized as follows. Section 2 describes the measurement campaign. The models including the heuristic and RT model are presented in Section 3. Section 4 compares the acoustic recordings with the numerical simulations. Finally, concluding remarks are provided in Section 5.

2. Measurement campaign

A dedicated acoustic measurement campaign was conducted to characterize aircraft flyover noise under realistic outdoor conditions at Morón Air Base, Spain, in September 2021. The experiment involved repeated flyovers of an aircraft (ATR 42–500) along a runway oriented 20°/200° with respect to magnetic north (0°), with takeoffs heading southward and landings northward. Aircraft trajectories, including position and speed, were accurately tracked using GPS throughout the campaign.

To capture acoustic data, two 4192-L-001 1/2" *Brüel & Kjær* microphones with Type 2669-L preamplifiers were deployed at the same location but at different heights to assess ground effect contributions: one microphone was flush-mounted at ground level $z = 0$ m, and the other was positioned at a height of $z = 1.2$ m above the ground. The microphones were placed on and above the runway, which extends several meters around them. The nearest obstacle is a small house located approximately 600 m away from the microphones.

In parallel, meteorological measurements were performed to estimate atmospheric propagation conditions. A ZX 300 scanning lidar (*ZX Lidars*) was used to obtain vertical wind profiles, providing information on wind speed and direction from 10 m to 300 m above ground level. For the ground level (z = 0 m), we assume that the wind speed is equal to zero. A spline interpolation is applied to obtain a continuous vertical profile between the measurement points. Above 300 m, the wind profile is extrapolated up to 1 km by continuing the trend observed at the highest measurement points, ensuring a smooth transition without abrupt changes in gradient.

To capture vertical temperature gradients, an instrumented drone performed in situ ascents, providing radiosonde measurements from the ground ($z = 0$ m) and up to $z = 1000$ m, with a 30 m discretization step.

The ground impedance was measured on site following the ANSI standard [27] and fitted using the slit-pore model [28]. The resulting values are a flow resistivity of 1057 kPa s m^{-2} and a porosity of 0.13.

The combination of acoustic, meteorological, ground impedance and trajectory data yields a dedicated dataset for analyzing the influence of atmospheric refraction, ground impedance, and Doppler effects on aircraft noise reception. Fig. 1 shows the runway, the locations of the microphones, as well as the lidar and the drone used during the campaign.

2.1. Wind and temperature vertical profiles

Wind and temperature vertical profiles were recorded concurrently with the acoustic measurements to characterize atmospheric propagation conditions. Fig. 2 shows the temperature and wind profiles measured respectively by the drone and by the lidar, as well as the wind direction measured by the lidar (wind direction relative to north). The colored curves highlight specific atmospheric conditions that will be referenced in Section 4 for comparison with numerical simulations from the RT model presented in Section 3. These three test-cases are chosen to span different propagation scenarios. The 19:20 case features low wind shear and a wind direction nearly transverse to the source–receiver axis, which is expected to reduce refraction effects in the source–receiver direction. The 20:00 case is characterized by a wind shear in the vertical profile, which may affect sound propagation. Finally, the 21:30 case exhibits the strongest wind speeds, with a wind direction aligned with the runway axis, potentially enhancing propagation effects due to wind. Regarding thermal conditions, it is important to note that temperature gradient measurements are only available at 20:15. Temperature remains nearly constant with height, varying by about 2 °C over 300 m.

2.2. Aircraft trajectories

Aircraft positions and velocities were recorded using onboard GPS, enabling precise reconstruction of flight trajectories during the measurement campaign. Fig. 3 displays the three-dimensional (3D) trajectories of the aircraft for takeoff procedures along the 20°/200° runway axis, while Fig. 4 presents the Mach number of the aircraft during the flight, defined as the ratio of the aircraft's velocity to the local sound speed. These selected trajectories correspond to the closest-in-time meteorological conditions shown in Fig. 2, and will serve as test-case trajectories in the comparative analysis presented in Section 4. The three trajectories

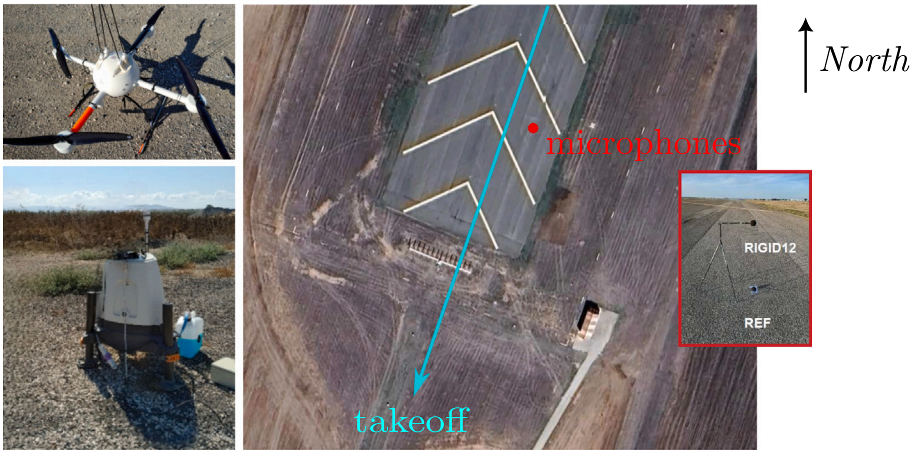

Fig. 1. Drone and lidar (left). Runway and microphone location (right).

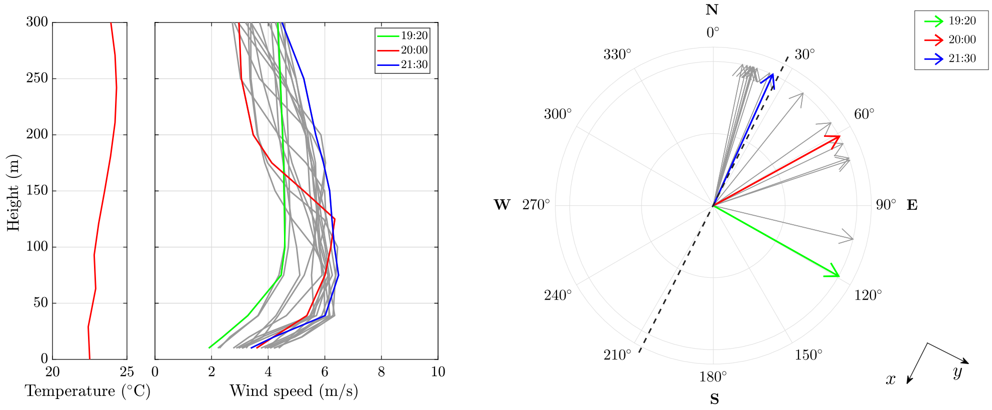

(a)

(b)

Fig. 2. Temperature profile measured by the drone ((a), left), wind speed profiles measured by the lidar ((a), right), and wind direction measurements from the lidar (b). The black dashed line indicates the runway orientation.

span different flight geometries: the 19:17 and 20:04 trajectories feature a gradual climb while the 21:29 trajectory starts at a lower altitude with a steeper ascent angle. This variety allows the analysis to encompass a broader range of source–receiver configurations and propagation conditions, including favorable and unfavorable meteorological situations (e.g., downward and crosswind propagation), as well as scenarios involving acoustic shadow zones.

2.3. Acoustic recording example

The spectrograms associated with the 19:17 test case are displayed in Fig. 5 for illustration. Time $t = 0$ s corresponds to the beginning of the recording. The audio signals acquired at a sampling frequency of 48 kHz are analyzed using a Hamming window of size 2048 points, with 50 % overlap between successive windows. The discrete Fourier transform was computed using 8192 points, applying zero-padding beyond the 2048-point window to produce a smoother spectrum and facilitate the visualization of spectral features.

At ground level $z = 0$ m in Fig. 5(a), interference patterns due to ground reflection are absent. At $z = 1.2$ m in Fig. 5(b), the interference minima and maxima can be seen in the measurements. These spectrograms allow for a comparative analysis of the spectral content and temporal evolution of the received noise at both microphone positions. Note that the displayed levels are normalized and do not reflect the absolute sound pressure levels measured during the campaign. The spectrograms provide a quick visual insight into the spectral content of the recorded acoustic signals. As expected, the acoustic energy is primarily concentrated in the low-frequency range, with a clear maximum occurring when the aircraft is perpendicular to the microphone ($t \approx 38$ s), corresponding to the moment of closest approach. The signal exhibits a broadband frequency content similar to pink noise, and no distinct tonal components are observed. Atmospheric absorption is also evident: high-frequency content is noticeably attenuated when the aircraft is farther from the receiver, both at early and late times. Additionally, weak stochastic variations are visible (for instance, at $t = 17$ s or 30 s) with sudden fluctuations in the pressure level which may be attributed to atmospheric turbulence effects (scattering), as well as ambient background noise. A narrowband component around 5 kHz is also noticeable on the spectrogram and is attributed to insect noise (mainly crickets) present during the measurements.

In addition to the time-frequency representations, the transfer function between the two microphone heights

$$T(x, y, f, t) = 10\log_{10}\left(\frac{|p^2(x, y, z = 1.2\text{ m}, f, t)|}{|p^2(x, y, z = 0\text{ m}, f, t)|}\right) \tag{1}$$

is also computed and presented in Fig. 5(c). If we assume that the aircraft is a compact source and that the difference in directivity and emission characteristics due to Doppler shift is negligible along the propagation paths, this transfer function does not depend on the source properties (directivity and frequency content) but on the aircraft trajectory and propagation effects only.

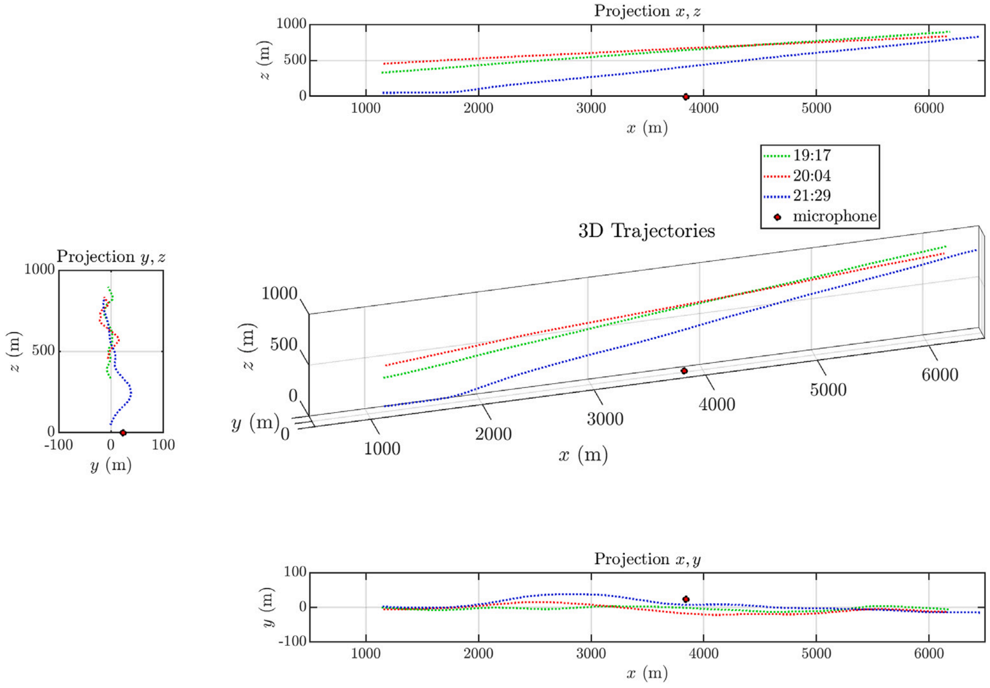

Fig. 3. Aircraft trajectories reconstructed from GPS data. The projection in each plane (xy, xz, and yz) is also plotted. The red dot shows the microphone position.

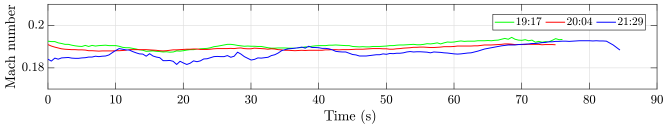

Fig. 4. Speed of the aircraft represented as Mach number for each of the test-case considered.

3. Models

3.1. Heuristic formulation for a monopole in arbitrary motion above a ground

In this section, we summarize the heuristic model [21] and the RT model, that were already introduced in Ref. [24]. We present equivalent but slightly modified formulations, that are better suited for calculating spectrograms for a broadband source. Integration of coherence loss due to atmospheric turbulence and scattering loss in the heuristic and the RT models is then described. Atmospheric absorption has also been accounted for in both models following ISO-9613 standard [29]. As we are primarily concerned with transfer functions between two closely spaced microphones for which atmospheric absorption does not play a role, the integration of atmospheric absorption in the models is not detailed.

3.1.1. Heuristic formulation considering a homogeneous atmosphere

A heuristic formulation has been proposed in the literature [21] to describe the sound field from a monopole in arbitrary motion above an absorbing ground surface and for a homogeneous and quiescent atmosphere. In this formulation, the ray paths are straight lines, as refraction is not taken into account, which is the main limitation of this approach (see sketch in Fig. 6). On the other hand, the heuristic formulation does consider the source motion effects: Doppler frequency shift and convective amplification, as well as ground effects. Note also that the original formulation of the heuristic model [21] includes acceleration terms that are neglected in this study as we consider source motion at constant speed in the following (see Section 3.2).

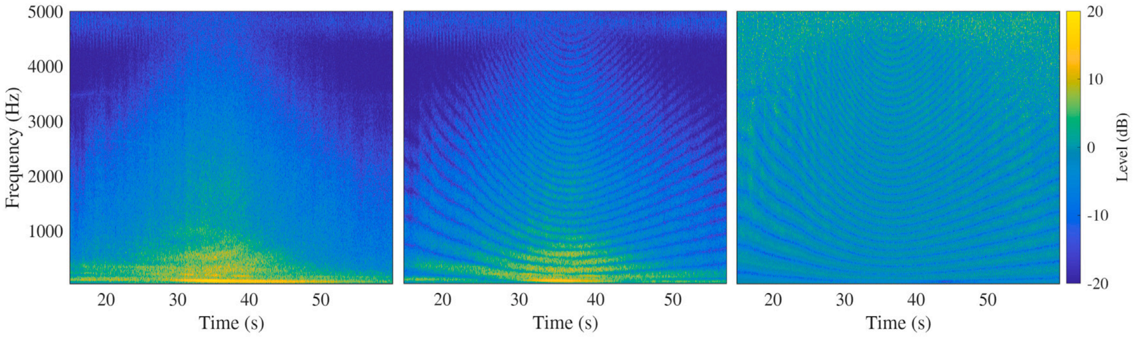

(a) (b) (c)

Fig. 5. Spectrograms of the acoustic signals recorded at ground level $z = 0$ m (a) and at $z = 1.2$ m (b) for the 19:17 test case. The transfer function between the two microphones is also plotted in (c).

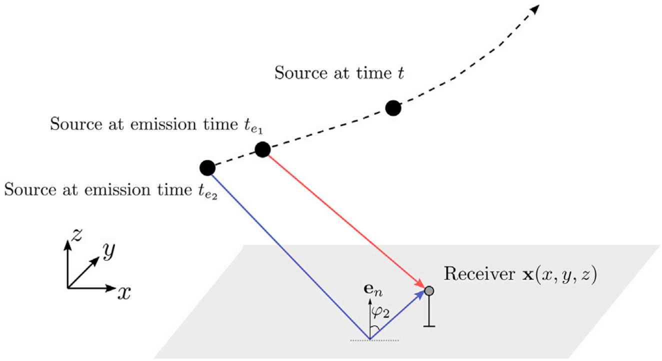

Fig. 6. Geometry considered for a moving monopole in arbitrary motion in a homogeneous atmosphere above a ground.

We consider the Cartesian system $\mathbf{x} = (x, y, z)$ and denote by t the time and by f the frequency at the receiver. We use the convention $\mathrm{e}^{-2\pi \mathrm{i} f t}$. The source trajectory is known: its position is denoted by $\mathbf{x_s}(t) = (x_s, y_s, z_s)$ and its speed by $\mathbf{V_s} = \mathrm{d}\mathbf{x_s}/\mathrm{d}t$. The source Mach number vector is $\mathbf{M_s} = \mathbf{V_s}/c_0$, with c_0 being the sound speed which is here assumed to be constant. We also introduce the image source position $\mathbf{x_{is}}(t) = (x_s, y_s, -z_s)$ and its corresponding Mach number $\mathbf{M_{is}}$. Note that the z-component of the Mach number vector associated with the image source is the opposite of that of the direct source, as the image source travels along the z-direction in the opposite direction to the direct source. We consider a broadband source with source strength $S(f_0)$, where f_0 is the source frequency. At the receiver, there are two contributions, the direct wave and the reflected wave. In the following, the index 1 refers to the direct wave and the index 2 to the reflected wave. The acoustic pressure at the receiver in the heuristic formulation is written as:

$$p(\mathbf{x}, f, t) = S(f_{01}) \frac{\mathrm{e}^{-\mathrm{i}2\pi f_{01} t_{e1}}}{R_{e1}(1 - M_{r1})^2} + S(f_{02}) Q \frac{\mathrm{e}^{-\mathrm{i}2\pi f_{02} t_{e2}}}{R_{e2}(1 - M_{r2})^2} \qquad (2)$$

with R_{e1} and R_{e2} being the distances between the source and the receiver and between the image source and the receiver at the emission times t_{e1} and t_{e2}. Thus, for the direct wave, one has $R_{e1} = |\mathbf{R_{e1}}|$ with $\mathbf{R_{e1}} = \mathbf{x} - \mathbf{x_s}(t_{e1})$. Similarly, for the reflected wave, one has $R_{e2} = |\mathbf{R_{e2}}|$ with $\mathbf{R_{e2}} = \mathbf{x} - \mathbf{x_{is}}(t_{e2})$. The emission time which is different for the direct and the reflected waves has to be determined numerically as a function of the time by solving the equation $t_e = t - R_e/c_0$.

The terms $(1 - M_r)^{-2}$ with $M_{r1} = \mathbf{M_s} \cdot \mathbf{R_{e1}}/R_{e1}$ and $M_{r2} = \mathbf{M_{is}} \cdot \mathbf{R_{e2}}/R_{e2}$ in Eq. (2) correspond to convective amplification effects, arising from the motion of the source. Note that the exponent in the convective amplification term depends on the source type: it is two for a monopole and a dipole but three for a quadrupole. As for atmospheric absorption, the convective amplification terms are expected to have a minor impact on the transfer function between two closely spaced microphones.

In addition, the term Q in Eq. (2) is the spherical-wave reflection coefficient which depends on the source–receiver geometry and on the normalized impedance of the ground Z. Specifically, one has:

$$Q = \mathcal{R} + (1 - \mathcal{R}) F(d), \qquad F(u) = 1 + \mathrm{i} u \sqrt{\pi} w(u), \qquad (3)$$

with w is the Faddeeva function. The plane-wave reflection coefficient $\mathcal{R}$ and the numerical distance d are given by:

$$\mathcal{R} = \frac{\cos\varphi_2 - 1/Z(f)}{\cos\varphi_2 + 1/Z(f)} \qquad d = \frac{1}{2}(1 + \mathrm{i}) \sqrt{\frac{2\pi f R_{e2}}{c_0}} (\cos\varphi_2 + 1/Z(f)). \qquad (4)$$

We note that the surface impedance has to be evaluated at the receiver frequency and not at the source frequency [25].

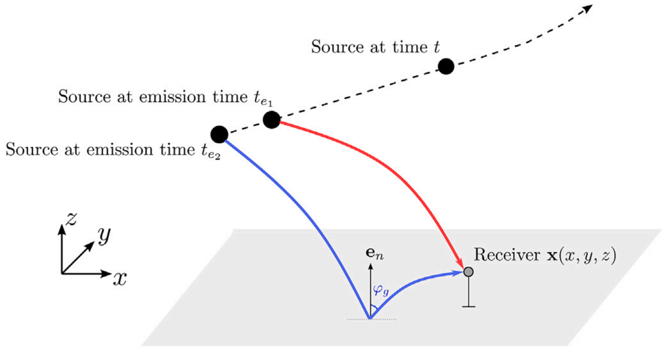

Fig. 7. Geometry considered for a moving monopole in arbitrary motion in an inhomogeneous atmosphere above a ground.

Finally, the source and receiver frequencies are related by the Doppler equations $f = f_{01}/(1 - M_{r1})$ and $f = f_{02}/(1 - M_{r2})$. It should be remarked that the component of frequency f at the receiver has not been emitted at the same frequency for the direct wave and the reflected wave because of the Doppler effect.

3.1.2. Ray-tracing formulation considering an inhomogeneous atmosphere

To simulate aircraft noise, it is necessary to consider a source in arbitrary motion within an inhomogeneous and moving atmosphere and above an absorbing ground. To achieve this, we have recently proposed and validated a formulation [24] based on the coupling of the heuristic formulation (Eq. (2)) that accounts for source motion and reflection from an absorbing ground and a ray-tracing method that considers refraction due to wind and temperature gradients.

Assuming that there are two rays reaching the receiver, the direct ray and the reflected ray, the acoustic pressure is expressed as:

$$p(\mathbf{x}, f, t) = S(f_{01}) A_1 \mathrm{e}^{-\mathrm{i}2\pi f_{01} t_{e1}} + S(f_{02}) Q A_2 \mathrm{e}^{-\mathrm{i}2\pi f_{02} t_{e2}}, \qquad (5)$$

with A being the wave amplitude. We also introduce τ the travel time from the source at the emission time t_e to the receiver at the time t, i.e. $\tau = t - t_e$.

The rays and the travel times are determined by solving the equations (see, e.g., [30–32]):

$$\frac{\mathrm{d}\mathbf{x}_r}{\mathrm{d}t_r} = c_0 \mathbf{n} + \mathbf{V_0} \qquad \frac{\mathrm{d}\mathbf{n}}{\mathrm{d}t_r} = (\mathbf{q} \cdot \mathbf{n})\mathbf{n} - \mathbf{q}, \qquad (6)$$

with $\mathbf{x}_r$ the ray position, $\mathbf{n}$ the local unit vector normal to the wavefront, t_r the travel time along the ray, $\mathbf{V_0}$ the wind velocity profile, and $\mathbf{q} = \nabla c_0 + (\nabla \mathbf{V_0}) \cdot \mathbf{n}$, where $(\nabla \mathbf{V_0}) \cdot \mathbf{n}$ is the directional derivative of the flow velocity vector. Note that c_0 can vary with space in this formulation. The rays are such that $\mathbf{x}_r(t_r = 0) = \mathbf{x_s}(t_e)$ and $\mathbf{x}_r(t_r = \tau) = \mathbf{x}$. Finally, the amplitudes A are obtained by computing the variation of the ray-tube area along the ray using the conservation of energy flux along a ray-tube. The reader may refer to Ref. [24] for further details on the method.

In Eq. (5), the spherical-wave reflection coefficient Q has the same form as in Eq. (3) but the plane-wave reflection coefficient and the numerical distance are modified as follows:

$$\mathcal{R} = \frac{\cos\varphi_g - 1/Z(f)}{\cos\varphi_g + 1/Z(f)} \qquad d = \frac{1}{2}(1 + \mathrm{i}) \sqrt{2\pi f \tau_2} [\cos\varphi_g + 1/Z(f)], \qquad (7)$$

with φ_g the angle of incidence of the ray on the ground (see Fig. 7). For an inhomogeneous and moving atmosphere, the relation between the source frequency and the receiver frequency is slightly more involved than for an inhomogeneous and quiescent atmosphere.

One has [33, Eq. (5.68)]:

$$f = f_0 \frac{1 + \mathbf{M_0}(0) \cdot \mathbf{n}(0)}{1 + [\mathbf{M_0}(0) - \mathbf{M_s}(0)] \cdot \mathbf{n}(0)}, \tag{8}$$

where the Mach number vector associated with the flow at the source position $\mathbf{M_0} = \mathbf{V_0}/c_0$ and the source Mach number vector are both evaluated at the emission time. In addition, $\mathbf{n}(0)$ is the unit vector normal to the wavefront of the emitted wave, determined from the ray tracing.

As a final remark, the RT model gives identical results to those of the heuristic model for a homogeneous and quiescent atmosphere.

3.2. *Description of the model setting*

The numerical simulations are conducted in a two-dimensional framework within the xz plane. The aircraft trajectory is approximated by a straight line obtained through linear regression of the original 3D data projected onto the xz plane. Similarly, the source Mach numbers are assumed constant and set to their average value computed over the duration of the trajectory. This simplification facilitates the modeling while retaining the essential characteristics of the aircraft motion's effect on acoustic propagation.

In the simulations, the wind orientation relative to the source–receiver direction is accounted for by applying a $\cos\theta$ weighting to the wind profile, where θ is the angle between the wind direction and the source–receiver axis (i.e., the x-axis). Furthermore, as the thermal gradient is weakly pronounced, the temperature T will be fixed at a constant average value T_0.

The ground surface impedance is computed using the *slit-pore* model [28] with an airflow resistivity of 1057 kPa s m^{-2} and a porosity of 0.13. These ground properties were measured on site and fitted using the *slit-pore* model. We remind the reader that the *slit-pore* model is a physically based impedance model and, as such, is physically admissible [34], contrary to semi-empirical models such as those of Delany and Bazley [35] or Miki [36], which may exhibit non-causal or non-passive behavior at low frequencies.

The numerical simulations are based on the aircraft trajectory as input. For comparison with the recordings, a reference time has to be chosen as the recordings were not synchronized with the aircraft trajectory. Here, we choose the instant at which the sound pressure level at the ground microphone is maximum. For each test case, a simulation with the ray-tracing model was carried out modeling the aircraft noise source as a pink noise. A time shift was then applied to the time vector describing the trajectory so that the maximum level aligns with that in the recording.

3.3. *Coherence loss due to atmospheric turbulence scattering*

Atmospheric turbulence significantly affects sound propagation, particularly in acoustic shadow zones where geometric acoustics predict no ray propagation [37]. Indeed, turbulence induced scattering of acoustic waves, attenuates the SPL at the interference maxima and increases the SPL at the interference minima, thereby mitigating the strong drop in SPL in these zones.

Regarding ray-tracing models, the average effect of scattering by atmospheric turbulence can be represented by the decorrelation between the direct and reflected rays. Earlier studies have proposed formulations for near-horizontal propagation [38], although their limitations were later discussed in Section 8.1 of [33], which, for the first time, introduced a coherence factor C_{coh} based on a von Kármán turbulence spectrum with parameters depending on the friction velocity u_* and the sensible heat flux Q_H. Ref. [26] extended these results to both near-horizontal and slanted propagation, accounting for statistically inhomogeneous turbulence where the spectrum Φ varies with height. In the present work, we adopt the formulation proposed in Ref. [26], which is suited to slant propagation conditions representative of aircraft fly-over configurations. A coherence factor C_{coh} is introduced as:

$$C_{\text{coh}}(f) = \exp\left(-\pi^2 \, k^2 \frac{(z_s - z)}{\sin\alpha_1} \int_0^1 \int_0^\infty \Phi[z_s - (z_s - z)\eta, \kappa] \right. \\ \left. [1 - J_0\,(r\,\kappa\,\eta)]\,\kappa\,\mathrm{d}\kappa\,\mathrm{d}\eta \right), \tag{9}$$

where $k = 2\pi f/c_0$ is the wavenumber, J_0 is the Bessel function of the first kind of order 0, z_s and z are the source and receiver heights, α_1 is the grazing angle of incidence for the direct path, and $r = 2\,z\cos\alpha_2$ with α_2 the grazing angle of incidence for the reflected path. This formulation is valid when α_1 and α_2 are greater than 25°. In our case, the propagation angles are much smaller during takeoff, but these conditions occur only for a short portion of the trajectory. We have chosen to retain the same formulation throughout to avoid introducing discontinuities in the spectrograms that would result from switching to an alternative formula for small angles. The double integral involves the function $\Phi(\xi,\kappa)$, which describes the contribution of turbulent fluctuations to the coherence loss and is expressed as:

$$\Phi(\xi,\kappa) = \frac{\Gamma\left(\frac{11}{6}\right)}{\pi^{3/2}\Gamma\left(\frac{1}{3}\right)} \left[\frac{\sigma_T^2(\xi)\,L_T^3(\xi)}{T_0^2\left(1+\kappa^2 L_T^2(\xi)\right)^{11/6}} + \frac{22}{3}\frac{\sigma_{V_s}^2\,L_{vs}^5(\xi)\,\kappa^2}{c_0^2\left(1+\kappa^2 L_{vs}^2(\xi)\right)^{17/6}} \right. \\ \left. + \frac{22}{3}\frac{\sigma_{V_b}^2\,L_{vb}^5\,\kappa^2}{c_0^2\left(1+\kappa^2 L_{vb}^2\right)^{17/6}} \right]. \tag{10}$$

Meteorological parameters such as the temperature scale T_* and friction velocity u_* are introduced via Monin–Obukhov Similarity Theory (MOST) [39]. The temperature variance σ_T^2 and velocity variances $\sigma_{V_s}^2$, $\sigma_{V_b}^2$ are computed accordingly, using the Obukhov length L_0 and length scales L_T, L_{vs}, and L_{vb} as defined in [26].

This formulation enables an estimation of coherence loss due to turbulence without relying on empirical adjustments, and is directly implemented numerically using a two-dimensional integration with the *trapz* function of *Matlab* software.

The coherence loss in Eq. (9) has been derived neglecting refraction and for a stationary source. For inclusion in the ray-tracing framework, the coherence loss is computed at each time step by evaluating z_s, α_1, and α_2 at the emission times. The resulting coherence factor C_{coh} is then used in the expression of the mean square pressure field at the receiver. For a source with unit source strength, this yields from Eq. (5):

$$\langle p^2\rangle(\mathbf{x}, f, t) = A_1^2 + |Q|^2 A_2^2 + 2C_{\text{coh}}(f,t)|Q|A_1 A_2 \cos\left[2\pi(f_{01}\,t_{e1} - f_{02}\,t_{e2}) + \Psi\right], \tag{11}$$

where Ψ is the phase of the spherical wave reflection coefficient Q. A similar formulation is also employed for the heuristic model. We can notice that the decorrelation induced by turbulence scattering does not modify the position of the interference dips in the spectrograms, as they occur when $2\pi(f_{01}\,t_{e1} - f_{02}\,t_{e2}) + \Psi = \pi + 2n\pi$, with n an integer, with or without coherence loss. However, it tends to reduce the depth of the interference dips.

In the following, we use classical values [33] for the MOST parameters, with a sensible heat flux set to $Q_h = 20$ W m^{-2} and a friction velocity of $u_* = 0.3$ m s^{-1} which are consistent with the observed conditions in field (clear sky on a summer evening).

Fig. 8 illustrates this decorrelation effect on the transfer function computed by the ray tracing model, considering the 19:17 test-case. Note that there is no coherence loss for the microphone at the ground as the direct and reflected paths are identical. In contrast, coherence loss affects the microphone located at a height of 1.2 m, and consequently, it also impacts the transfer function. The coherence loss caused by turbulence scattering between direct and reflected rays is visible for both

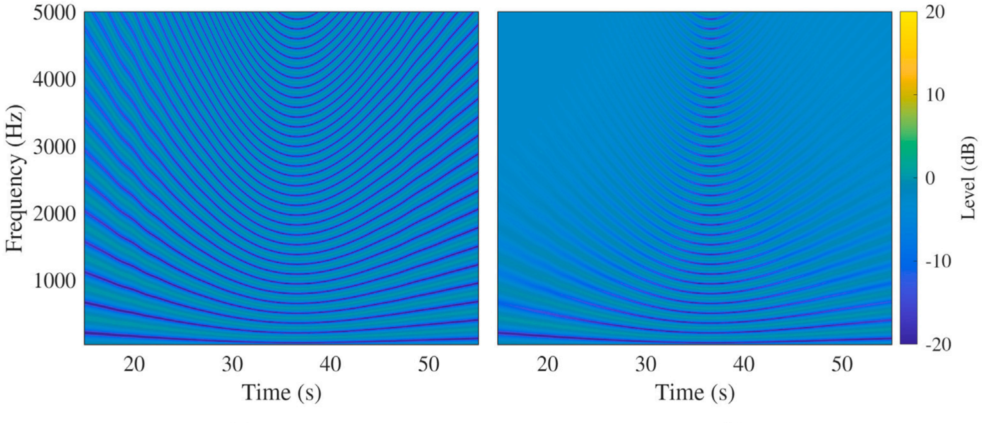

(a) (b)

Fig. 8. Numerically computed transfer function without turbulence (a) and with turbulence (b).

short ($t < 35$ s) and long ($t > 45$ s) travel times. This effect becomes more pronounced at higher frequencies, where the phase sensitivity to atmospheric fluctuations increases. In contrast, the impact of turbulence is negligible in near-vertical propagation cases, where ray paths remain closely aligned.

4. Comparison of simulations and *in-situ* measurements

This section presents a comparison between the acoustic measurements and numerical simulations. This comparison aims to assess the ability of the ray-tracing model to accurately simulate the acoustic propagation, including refraction effects, source motion effects and ground effects. The three selected test cases, recorded respectively at 19:17, 20:04, and 21:29, are chosen to represent different atmospheric conditions observed during the campaign. The two models introduced in Section 3.1 are compared with the measured acoustic data: a simplified heuristic formulation that ignores atmospheric refraction, and the ray-tracing model that considers wind and temperature profiles.

4.1. Ray-tracing approach

Fig. 9 illustrates the ray-tracing simulations corresponding to each test-case, along with the associated wind profiles. To reduce computational cost, ray paths are computed by launching rays from the receiver rather than from the source, using a reversed wind profile. This approach relies on the flow reversal theorem [40], which is a generalized acoustic reciprocity principle for a moving medium and ensures that the acoustic path from source to receiver is identical to that from receiver to source if the flow is reversed. This method avoids the computation of ray paths for each source position along the aircraft trajectory.

Fig. 9 also provides a first insight into the propagation effects. For 19:17, the rays are almost straight, implying that refraction effects are expected to be negligible. The ray structure for 20:04 and 21:29 is similar. A shadow zone is formed for $x < 0$ and has almost the same boundary for both cases. Downward refraction can be observed for rays launched rightwards that propagate along the ground. The main difference between the cases 20:04 and 21:29 is the aircraft trajectory. Indeed, since the aircraft at 21:29 is flying closer to the ground and crosses the shadow zone boundary, propagation effects are expected to be more significant in this case. It is worth noting that a known limitation of the ray-based approach is its inability to provide any information within shadow zones, where no rays reach the receiver. This limitation is particularly evident here at early times (left side of the plots) for the 21:29 test-case.

4.2. Principle and application of the numerical transfer function between microphone positions

To evaluate the RT model, the transfer function between the two microphone positions ($z = 0$ m and $z = 1.2$ m) is computed using the model. For the purpose of the comparison, the computed transfer functions are applied to the spectrogram measured at $z = 0$ m to simulate the corresponding spectrogram at $z = 1.2$ m. These results are then compared to the actual measurements at $z = 1.2$ m to assess the precision of each model under various atmospheric conditions. Fig. 10 illustrates this principle for the 19:17 test-case.

4.3. Spectrogram comparison

This section compares the measured spectrograms at $z = 1.2$ m with those obtained from the measurements at $z = 0$ m and the numerical transfer function (see explanations in Section 4.2).

Figs. 11–13 show the spectrograms for the three test-cases (19:17, 20:04 and 21:29). Overall, the methodology using both the heuristic or the RT model faithfully reproduces the spectrogram at a height of 1.2 m. As the RT model considers acoustic refraction, the position and the curvature of the interference patterns are better captured, particularly when the aircraft approaches or recedes from the microphones in scenarios involving slant acoustic propagation ($t < 30$ s and $t > 40$ s). When the aircraft is positioned perpendicularly to the microphone ($30 \text{ s} < t < 40$ s), corresponding to the moment of the shortest source–receiver distance, the effects of refraction are less influential due to near-vertical propagation, resulting in closer outcomes between the RT model and the simplified heuristic model. Thus, while the difference with the heuristic model remains moderate, the RT model provides improved agreement with the measured spectrograms, particularly in configurations involving non-vertical sound propagation.

In more detail, for 19:17 in Fig. 11, the heuristic and RT models give almost the same results, as refraction effects are small in this case. For 20:04 in Fig. 12, the interference patterns in the RT model closely match those in the measurements. In particular, the white dashed lines aligned with some interference dips in the measurements are similarly aligned with those in the RT model. In the heuristic model, a small shift in the interference patterns is observed for $t < 30$ s and for $t > 40$ s. Finally, for 21:29 in Fig. 13, the propagation effects are the more pronounced. The RT model reproduces accurately the interference dips. We note also that the aircraft is in the shadow zone for $t < 26$ s implying that the RT model is not able to predict the sound pressure in this configuration (see Fig. 13(b)). Concerning the heuristic model, we observe that outside the range $38 \text{ s} < t < 45$ s the interference patterns are shifted with respect to those in the measurements. This is particularly noticeable for

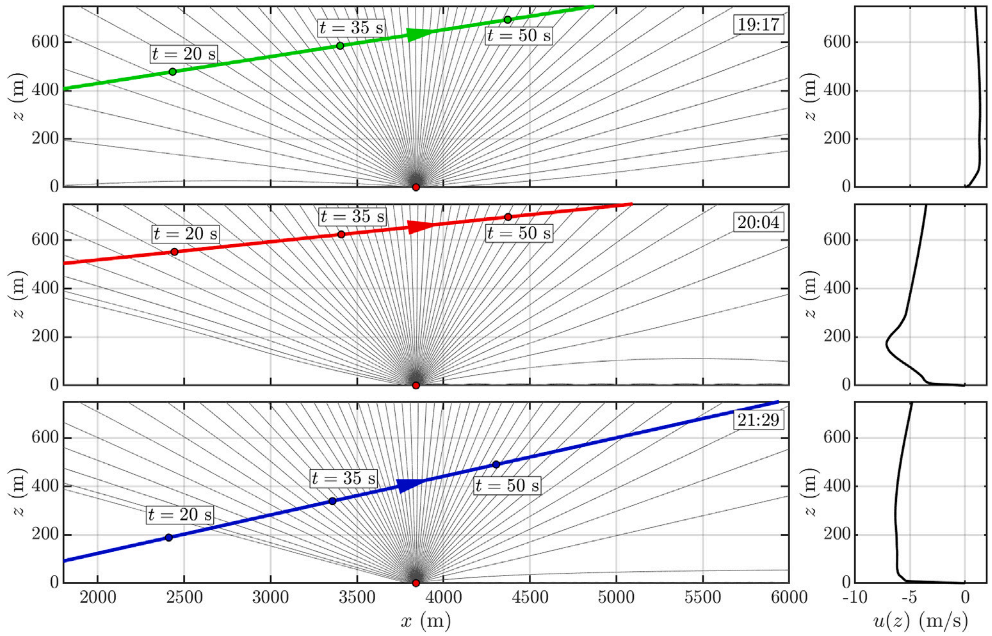

Fig. 9. (left) Ray trajectories in gray thin lines launched from the ground microphone shown with a red dot for the three configurations. The associated aircraft trajectory is also plotted in colored thick line and its position at three instants in time is indicated by a colored dot. (right) Corresponding wind speed profile in the propagation plane.

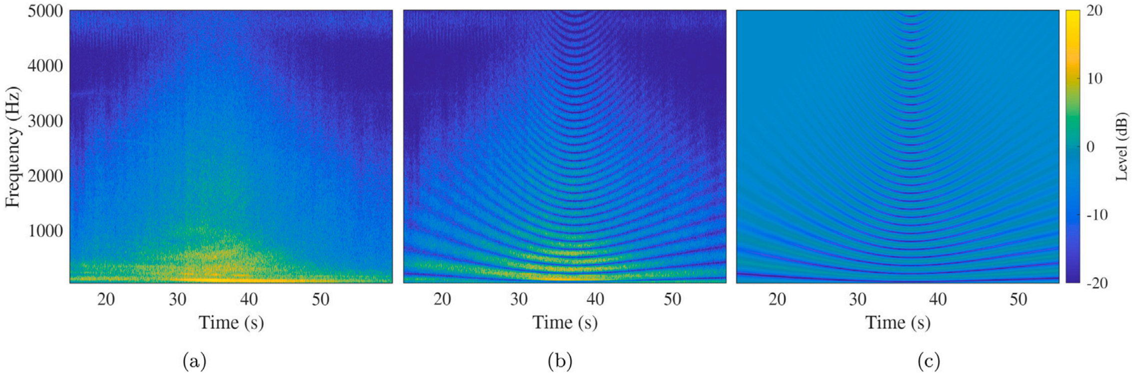

Fig. 10. Application of a numerically computed transfer function (c) to the spectrogram measured at ground level $z = 0$ m (a) to estimate the spectrogram at $z = 1.2$ m (b) for the 19:17 case study.

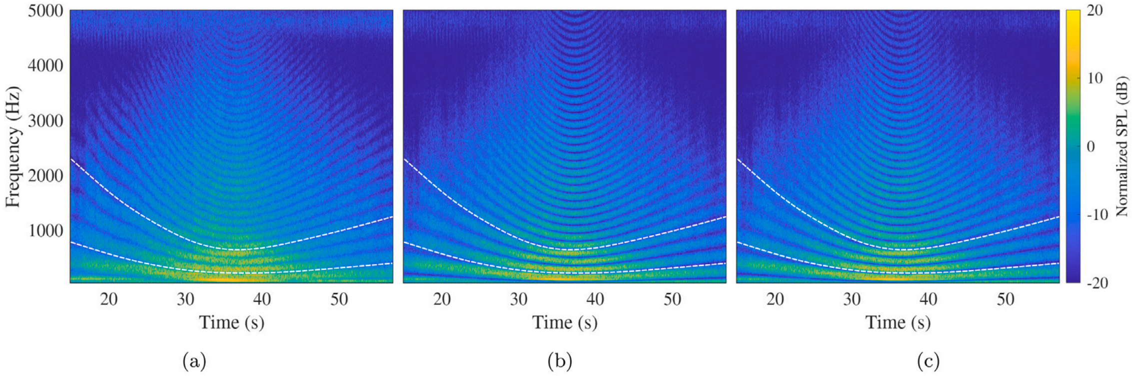

Fig. 11. Comparison of spectrograms for the 19:17 test-case: experimental recording (a), RT model (b), and simplified heuristic model (c). Fixed white dashed lines are included across all three spectrograms to facilitate visual comparison.

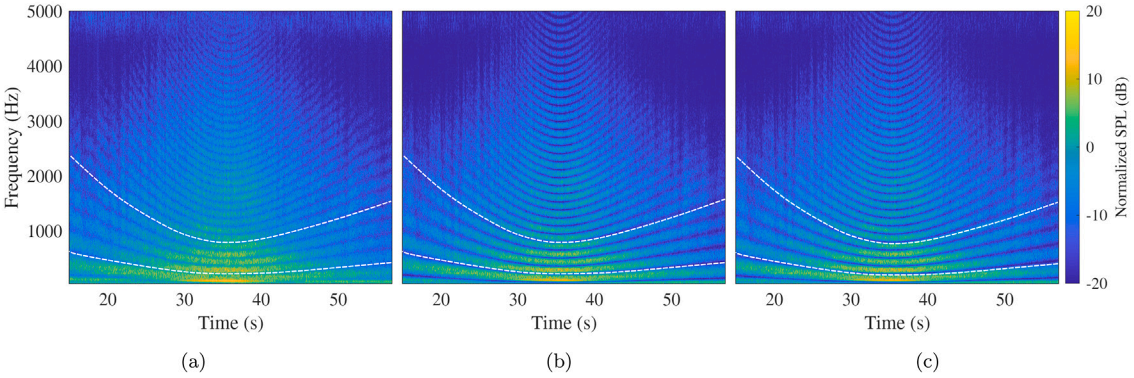

Fig. 12. Comparison of spectrograms for the 20:04 test-case: experimental recording (a), RT model (b), and simplified heuristic model (c). Fixed white dashed lines are included across all three spectrograms to facilitate visual comparison.

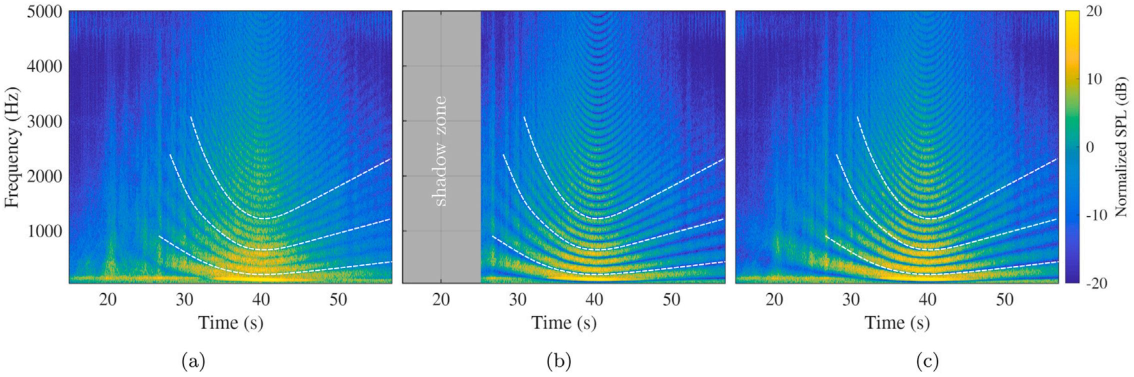

Fig. 13. Comparison of spectrograms for the 21:29 test-case: experimental recording (a), RT model where the empty part correspond to the shadow zone (b), and simplified heuristic model (c). Fixed white dashed lines are included across all three spectrograms to facilitate visual comparison.

26 s $< t <$ 32 s. Naturally, the heuristic model does not suffer from the limitation of the RT model in the shadow zone and provides information for $t <$ 26 s. However, the effect of the shadow zone is also visible in the experiments in Fig. 13(a) for $t <$ 26 s with the suppression of the interference dips, while the heuristic model still predicts interference dips at low frequencies (interference patterns are not observed at higher frequencies due to atmospheric turbulence accounted for in the models).

4.4. Transfer functions comparison

Fig. 14 compares the transfer functions between the microphones at two selected instants in time, allowing for a more quantitative analysis than in Section 4.3. These instants correspond to two representative configurations: the first one where the aircraft is nearly perpendicular to the microphones (refraction effects are small), and the second one at a later time when the aircraft is farther away (refraction effects are significant).

At first glance, the measured transfer functions exhibit noticeable fluctuations, which can be attributed to background noise, atmospheric scattering, and measurement uncertainties. In contrast, the numerically computed transfer functions appear much sharper, particularly in the absence of stochastic perturbations.

Let us focus the analysis on the interference patterns. In the case of vertical propagation, the heuristic and ray-based simulations yield similar results, as previously observed in the spectrograms, which closely match the measurements. For slant propagation, a correct agreement between the models and the experiments is also observed. The positions of the interference minima are generally better predicted by the ray-based model, due to its ability to account for atmospheric refraction which modifies the propagation paths. This is particularly noticeable in Fig. 14 for the cases 20:04 and 21:29 at t = 55 s. Nevertheless, the levels are not perfectly reproduced, especially at interference pattern minima. This can be explained by the presence of background noise at the site and by atmospheric turbulence. The turbulence effect in the model is represented by an ensemble average over several realizations, while the experimental data correspond by definition to a single realization, which naturally leads to discrepancies. Additionally, in the measurements, the spectrograms are averaged in frequency due to the finite window size and overlap. The frequency bandwidth is also finite. As a consequence, the data post-processing tends to smooth the interference dips, which makes them appear less sharp than in the model based on monochromatic calculations.

The inclusion of atmospheric turbulence in the simulations leads to a progressive smoothing of the interference pattern as frequency increases. This effect is less apparent in the measurements, likely due to the background noise level obscuring the effect of atmospheric turbulence scattering.

Overall, the slight discrepancies between the RT model simulations and the measurements can be attributed to several simplifications in the modeling process. The turbulence parameters were set to physically reasonable values based on the experimental context, but were not directly measured during the campaign, leaving room for refinement. Furthermore, the simulations assume a simplified 2D scenario in which the aircraft flies within the vertical plane above the microphone's position. In practice, slight lateral deviations in the aircraft's trajectory may introduce three-dimensional propagation effects that are not captured by the simulations.

It is worth noting that this study was limited to three experimental cases under specific, uncontrolled meteorological conditions. While further comparisons would be valuable, the RT model consistently

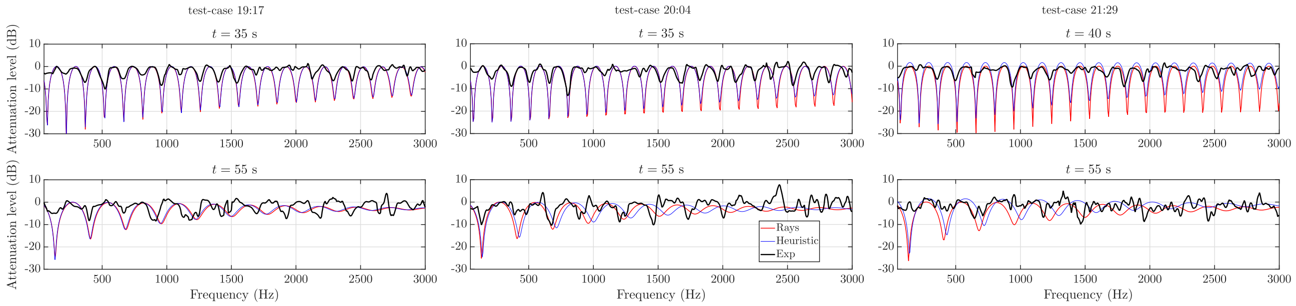

(a) (b) (c)

Fig. 14. Transfer function between the two microphones for cases (a) 19:17, (b) 20:04, and (c) 21:29. Vertical slices are shown at two instants in time.

shows improved accuracy. The heuristic model remains adequate for scenarios involving quasi-vertical propagation and limited atmospheric stratification.

5. Conclusion

In previous work, we introduced a coupled model combining a ray-tracing approach with a heuristic formulation to account for the main physical phenomena affecting outdoor sound propagation from moving sources (including ground effects, meteorological effects, convective amplification, and Doppler shift) and validated it against numerical benchmarks. In the present study, we extend this validation by comparing the predictions of the model with experimental data.

The experimental campaign involved aircraft flyovers above two microphones. One is placed directly on the ground and the other is elevated at 1.2 meters. Concurrent ground impedance measurements and meteorological measurements are conducted, which include wind speed and wind direction with a lidar, as well as a temperature profile with a dedicated drone that performed vertical take-off. The results of the comparison show that the coupled RT-heuristic model is in better agreement with the measured data than the classical heuristic approach. The latter shows limitations in reproducing the observed interference patterns, because it neglects atmospheric refraction, which bends the ray paths and significantly influences sound propagation. It is important to note that when the aircraft is at the normal of the microphone (which was the shortest source–receiver distance in our study) the results are similar between the RT model and the heuristic model.

Nonetheless, a known limitation of ray-based methods is their inability to account for acoustic propagation in shadow zones, where no ray paths connect the source to the receiver. In the present RT model, although atmospheric turbulence is partially considered in interference regions through the decorrelation of direct and reflected waves, its effect is not yet accounted for in shadow zones where the scattering induced by turbulence could contribute to the diffusion of acoustic energy.

This comparison highlights the greater accuracy of the RT model in presence of an inhomogeneous and moving atmosphere as it takes into account meteorological effects on sound propagation. This could be particularly crucial in the context of certification, especially if the aircraft emits tonal components that may alternately align with pressure maxima or minima induced by ground effects, potentially leading to significant variations in the resulting noise indicator.

As the proposed model better integrates atmospheric effects while remaining computationally efficient (with a typical computation time of a few hours on a standard laptop), it sets the stage for further sensitivity studies aimed at quantifying and ranking the influence of physical parameters, such as source trajectory, atmospheric stratification, and ground impedance, on noise propagation. Such analyses will help identify the dominant factors that affect sound levels at the receiver and thus guide efforts toward the design of more robust measurement standards for aircraft noise.

CRediT authorship contribution statement

Bill Kayser: Writing – original draft, Investigation, Conceptualization. **Didier Dragna:** Writing – review & editing, Supervision, Conceptualization.

Declaration of competing interest

The authors declare that they have no known competing financial interests or personal relationships that could have appeared to influence the work reported in this paper.

Acknowledgments

The present work is part of the program MAMBO “Méthodes avancées pour la modélisation du bruit moteur et avion” (Advanced methods for engine and aircraft noise modeling) coordinated by Airbus SAS. It was supported by the Direction Générale de l’Aviation Civile (DGAC) under the Grant no. 2021-50. It was also performed within the framework of the LABEX CeLyA (ANR-10-LABX-0060) of Université de Lyon, within the program “Investissements d’Avenir” (ANR-16-IDEX-0005) operated by the French National Research Agency (ANR).

Data availability

Data will be made available upon request.

References

[1] Arntzen M, Heblij SJ, Simons DG. Weather-dependent airport noise contour prediction concept based on ray tracing. J Aircr 2014;51(5):1351–9. https://doi.org/10.2514/1.C032149

[2] Tuinstra M. A fast atmospheric sound propagation model for aircraft noise prediction. Int J Aeroacoust 2014;13(5–6):337–61. https://doi.org/10.1260/1475-472X.13.5-6.337

[3] Wu C, Redonnet S. Aircraft noise impact prediction with incorporation of meteorological effects. Transp Res D Transp Environ 2023;125:103945. https://doi.org/10.1016/j.trd.2023.103945

[4] Yunus F, Casalino D, Avallone F, Ragni D. Toward inclusion of atmospheric effects in the aircraft community noise predictions. J Acoust Soc Am 2021;150(2):759–68. https://doi.org/10.1121/10.0005733

[5] Serafini J, Bernardini G, Grignaffini G, Modini S, Gennaretti M. Acoustic wave three-dimensional ground reflection and bouncing. Appl Acoust 2021;180:108110. https://doi.org/10.1016/j.apacoust.2021.108110

[6] Arntzen M, Rizzi SA, Visser HG, Simons DG. Framework for simulating aircraft flyover noise through nonstandard atmospheres. J Aircr 2014;51(3):956–66. https://doi.org/10.2514/1.C032049

[7] Schäfer P, Vorländer M. Atmospheric ray tracing: an efficient, open-source framework for finding eigenrays in a stratified, moving medium. Acta Acust 2021;5:26. https://doi.org/10.1051/aacus/2021018

[8] Schäfer P, Fatela J, Vorländer M. Interpolation of scheduled simulation results for real-time auralization of moving sources. Acta Acust 2024;8:9. https://doi.org/10.1051/aacus/2023070

[9] Arntzen M, Simons DG. Ground reflection with turbulence induced coherence loss in flyover auralization. Int J Aeroacoust 2014;13(5–6):449–62. https://doi.org/10.1260/1475-472X.13.5-6.449

[10] Pieren R, Lincke D. Auralization of aircraft flyovers with turbulence-induced coherence loss in ground effect. J Acoust Soc Am 2022;151(4):2453–60. https://doi.org/10.1121/10.0010121

[11] Lincke D, Pieren R. Auralization of atmospheric turbulence-induced amplitude fluctuations in aircraft flyover sound based on a semi-empirical model. Acta Acust 2024;8:47. https://doi.org/10.1051/aacus/2024036

[12] Bousquet P, Blandeau VP. Feasibility of determining aircraft certification noise levels using ground plane microphone measurements, in: Proceedings of AIAA AVIATION 2021 FORUM, Virtual Event, 2–6 August 2021, AIAA 2021-2159. https://doi.org/10.2514/6.2021-2159.

[13] Nesbitt E, Lan J, Hunkler S. Microphone acoustic characteristics for aircraft flyover testing. In: Proceedings of AIAA AVIATION 2020 FORUM, Virtual Event, 15–19 June 2020. AIAA 2020-2613. https://doi.org/10.2514/6.2020-2613

[14] Giannakis JM. Evaluation of a correction factor for flyover-noise ground plane microphones, in: Proceedings of AIAA AVIATION 2020 FORUM, Virtual Event, 15–19 June 2020, AIAA 2020-2612. https://doi.org/10.2514/6.2020-2612

[15] Blandeau VP, Bousquet P. A new plate design to improve the accuracy of aircraft exterior noise measurements on the ground, in: Proceedings of AIAA AVIATION 2021 FORUM, Virtual Event, 2–6 August 2021, AIAA 2021-2158. https://doi.org/10.2514/6.2021-2158

[16] Kingan MJ, Go ST, Piscoya R, Ochmann M. On the modelling of ground-board mounted microphones for outdoor noise measurements. J Sound Vib 2023;565. https://doi.org/10.1016/j.jsv.2023.117894

[17] Norum T, Liu C. Point source moving above a finite impedance reflecting plane—experiment and theory. J Acoust Soc Am 1978;63(4):1069–73. https://doi.org/10.1121/1.381839

[18] Oie S, Takeuchi R. Sound radiation from a point source moving in parallel to a plane surface of porous material. Acta Acust 1981;48(3):123–9.

[19] Ochmann M. Exact solutions for sound radiation from a moving monopole above an impedance plane. J Acoust Soc Am 2013;133(4):1911–21. https://doi.org/10.1121/1.4794389

[20] Li KM, Wang Y. On the three-dimensional sound fields from a moving monopole source above a non-locally reacting ground. J Acoust Soc Am 2020;147(4):2581–96. https://doi.org/10.1121/10.0001086

[21] Attenborough K, Van Renterghem T. Predicting outdoor sound. CRC Press; 2021. https://doi.org/10.1201/9780429470806

[22] Dragna D, Blanc-Benon P, Poisson F. Modeling of broadband moving sources for time-domain simulations of outdoor sound propagation. AIAA J 2014;52(9):1928–39. https://doi.org/10.2514/1.J052672

[23] Dragna D, Blanc-Benon P. Towards realistic simulations of sound radiation by moving sources in outdoor environments. Int J Aeroacoust 2014;13(5–6):405–26. https://doi.org/10.1260/1475-472X.13.5-6.405

[24] Kayser B, Dragna D, Blanc-Benon P. Heuristic solution for the acoustic radiation of a moving monopole in an inhomogeneous and moving atmosphere. Application to aircraft noise. Acta Acust 2024;8:62. https://doi.org/10.1051/aacus/2024048

[25] Dragna D, Blanc-Benon P. Sound radiation by a moving line source above an impedance plane with frequency-dependent properties. J Sound Vib 2015;349:259–75. https://doi.org/10.1016/j.jsv.2015.03.033

[26] Ostashev VE, Breton DJ, Wilson DK. Interference of the direct and ground-reflected waves in the atmosphere with volumetric scattering. J Acoust Soc Am 2024;156(1):107–18. https://doi.org/10.1121/10.0026452

[27] ANSI/ASA S1.18-2018. Method for determining the acoustic impedance of ground surfaces. New York: Acoustical Society of America; 2018.

[28] Attenborough K, Bashir I, Taherzadeh S. Outdoor ground impedance models. J Acoust Soc Am 2011;129(5):2806–19. https://doi.org/10.1121/1.3569740

[29] ISO9613-1:1993. Acoustics — sound attenuation in free field — part 1: atmospheric absorption calculation. Geneva, Switzerland: International Organization for Standardization; 1993.

[30] Candel SM. Numerical solution of conservation equations arising in linear wave theory: application to aeroacoustics. J Fluid Mech 1977;83(3):465–93. https://doi.org/10.1017/S0022112077001293

[31] Scott J, Blanc-Benon P, Gainville O. Weakly nonlinear propagation of small-wavelength, impulsive acoustic waves in a general atmosphere. Wave Motion 2017;72:41–61. https://doi.org/10.1016/j.wavemoti.2016.12.005

[32] Pierce AD. Acoustics: an introduction to its physical principles and applications. Springer; 2019. https://doi.org/10.1007/978-3-030-11214-1

[33] Ostashev VE, Wilson DK. Acoustics in moving inhomogeneous media. CRC Press; 2015. https://doi.org/10.1201/b18922

[34] Dragna D, Attenborough K, Blanc-Benon P. On the inadvisability of using single parameter impedance models for representing the acoustical properties of ground surfaces. J Acoust Soc Am 2015;138(4):2399–413. https://doi.org/10.1121/1.4931447

[35] Delany ME, Bazley EN. Acoustical properties of fibrous absorbent materials. Appl Acoust 1970;3(2):105–16. https://doi.org/10.1016/0003-682X(70)90031-9

[36] Miki Y. Acoustical properties of porous materials-modifications of Delany-Bazley models. J Acoust Soc Jpn E 1990;11(1):19–24. https://doi.org/10.1250/ast.11.19

[37] Salomons EM. Computational atmospheric Acoustics. Netherlands: Kluwer Academic; 2001.

[38] Clifford SF, Lataitis RJ. Turbulence effects on acoustic wave propagation over a smooth surface. J Acoust Soc Am 1983;73(5):1545–50. https://doi.org/10.1121/1.389416

[39] Monin A, Obukhov A. Basic laws of turbulent mixing in the surface layer of the atmosphere, TR. Akad Nauk SSSR Geophiz Inst 1954;24(151):163–87.

[40] Godin OA. Reciprocity and energy theorems for waves in a compressible inhomogeneous moving fluid. Wave Motion 1997;25(2):143–67. https://doi.org/10.1016/S0165-2125(96)00037-6